https://doi.org/10.5194/egusphere-2026-2297
Preprint. Discussion started: 5 June 2026

A deep-atmosphere extension in a nonhydrostatic dynamical core: formulation and idealized tests

Qitao Cui[1,2], Li Dong[1,3] and Bin Wang[1,3]

[1]National Key Laboratory of Earth System Numerical Modelling and Application, Institute of Atmospheric Physics, Chinese Academy of Sciences, Beijing 100029, China
[2]College of Earth and Planetary Sciences, University of Chinese Academy of Sciences, Beijing 100049, China
[3]College of Marine Sciences, University of Chinese Academy of Sciences, Qingdao 266400, China

Correspondence to: Li Dong (dongli@lasg.iap.ac.cn)

Abstract: We have developed a deep-atmosphere extension within the GMCORE (Grid-Model dynamical CORE) using a dry terrain-following mass-based coordinate. The new dycore retains the full three-dimensional Coriolis force, accounts for the height dependence of gravity, and introduces radial metric corrections into the discrete operators, while preserving the main structure of the original solver. Two idealized test cases are used for evaluation: a baroclinic wave test and a tropical cyclone test. In the standard Earth-radius baroclinic wave experiment, the deep- and shallow-atmosphere solutions are similar, whereas in the reduced-radius X20 configuration the GMCORE deep-atmosphere dycore reproduces the clear separation reported in earlier studies. In the tropical-cyclone experiment, the deep-atmosphere configuration has little effect on storm intensity and warm core structure, but leads to a systematic south-westward trajectory shift relative to the shallow-atmosphere simulation. The trajectory difference is linked to an organised inner asymmetry. This includes a dipole-like pattern connected to $2\Omega\cos\phi\frac{\partial w}{\partial y}$ and a low-level easterly anomaly. These results demonstrate that GMCORE can be extended to a deep-atmosphere dycore and provide a useful work for idealized tropical cyclone trajectory sensitivity and deep-atmosphere dynamics.

1 Introduction

Modern global atmospheric models are extending their upper boundaries into the mesosphere and lower thermosphere, motivating the use of deep-atmosphere dynamics. High-top models, for example, the WACCM (Whole Atmosphere Community Climate Model, Version 6) extends to approximately 140 km (Gettelman et al., 2019), while its thermosphere-ionosphere extension version (WACCM-X) extends to nearly 500 km (Liu et al., 2018). In addition, global nonhydrostatic dycores such as NICAM (Satoh et al., 2008), the Met Office model ENDGame (Wood et al., 2014), MPAS-A (Skamarock et al., 2021), ICON (Borchert et al., 2019), NUMA (Kelly et al., 2026) and CliMA (Yatunin et al., 2026) have introduced deep-atmosphere modifications to support the full equations and upper atmosphere simulations.

https://doi.org/10.5194/egusphere-2026-2297
Preprint. Discussion started: 5 June 2026

As models extend into higher layers, the shallow-atmosphere approximation becomes less accurate because the atmosphere vertical scale becomes not negligible compared to earth radius (White and Bromley, 1995; Akmaev, 2011). In practical modelling, the shallow-atmosphere approximation is commonly accompanied with traditional approximation, by neglecting horizontal component of the planetary rotation and curvature terms in order to preserve angular momentum (Phillips 1966; Vallis, 2017). While these omissions are usually small in the lower atmosphere, their importance increases with height and may become more significant in simulations involving large-scale flow and wave propagation in the upper atmosphere (Baldwin and Dunkerton, 2001; Fritts and Alexander, 2003; Kim et al., 2003).

The deep-atmosphere equations can be viewed as an extension of the traditional shallow-atmosphere equations, which relax a set of approximations involving spherical geometry, gravity and planetary rotation and change normal mode structure on vertical (Thuburn, 2002a; White et al., 2005). Among these differences, when the model top is not very high, the nontraditional Coriolis terms (NCTs)—which are neglected in the shallow-atmosphere equations—often play a significant role in the atmospheric motion (Colin de Verdière and Schopp, 1994; Marshall et al., 1997; Gerkema et al., 2008). Standard shallow-atmosphere equations project the planetary rotation vector onto the local vertical and neglect the horizontal component, simplifying the full rotation to the traditional Coriolis term $2\Omega\sin\phi$. However, a deep-atmosphere treatment retains the full rotation vector, including the components proportional to $2\Omega\cos\phi$, which couple horizontal and vertical motions.

A growing body of work has demonstrated that such NCTs can be numerically significant, especially in the tropics where the horizontal component of planetary rotation becomes comparable to other dynamical terms and affects wave dispersion and balance relationships (Gerkema et al, 2008; Ong and Roundy, 2019; Igel and Biello, 2020). By eliminating the Coriolis simplifications, the deep-atmosphere equations more truly represent rotational influences across latitudes, ensuring a consistent description of vortical and wave motions in a stratified, rotating atmosphere.

In this study, we develop a deep-atmosphere version based on GMCORE (Grid-Model dynamical CORE). GMCORE is a fully compressible nonhydrostatic dycore formulated on a latitude–longitude C grid with a dry terrain-following mass-based coordinate (Li et al., 2020; Li and Dong, 2024), and has been applied to Mars climate simulation researches (Dong et al., 2024; Liu et al., 2025). Our goal is to extend the original shallow-atmosphere dycore so that it retains the full three-dimensional Coriolis force, allows gravity to vary with height, and accounts for the radial dependence of metric terms in the discrete operators, while preserving the basic structure of the existing solver. An important feature of the present formulations is that the deep-atmosphere extension is represented within the dry terrain-following mass-based coordinate while most models use height-based vertical coordinate (Wood and Staniforth, 2003).

To evaluate the new dycore, we use two idealized test cases. The first is the deep baroclinic-wave test case (Ullrich et al, 2014), which is used here primarily as a validity check case. As emphasized by Skamarock et al. (2021), the interpretation of the X20 experiment is not straightforward because part of the reported deep-shallow differences may arise from differences in the analytic initial states rather than directly from the temporal integration of the two equation sets (Staniforth and White, 2011). We therefore use this case mainly to assess whether the GMCORE deep-atmosphere dycore reproduces the canonical numerical behaviour reported in the literature. The second test is an idealized tropical-cyclone test case (Reed and Jablonowski,

https://doi.org/10.5194/egusphere-2026-2297
Preprint. Discussion started: 5 June 2026

2011), which is used to examine the performance of the dycore in a strongly rotating, vertically deep, low-latitude vortex. Compared with the baroclinic-wave test, this case is also useful for discussing how the retention of the full Coriolis vector may influence storm trajectory and asymmetric structure.

The paper is organized as follows. Section 2 describes the governing equations of the deep-atmosphere GMCORE and its numerical implementation in the dry terrain-following mass-based coordinate. Section 3 presents results from the idealized baroclinic-wave and tropical-cyclone tests. Section 4 summarizes the main findings and discusses their implications and limitations.

2. Model description

2.1. The deep-atmosphere governing equations

Following Wood and Staniforth (2003) and other deep-atmosphere formulations (Borchert et al., 2019; Skamarock et al., 2021), GMCORE solves the fully compressible, nonhydrostatic deep-atmosphere equations in a dry terrain-following mass-based coordinate in vector-invariant form. Compared to the shallow-atmosphere equations, the deep extension introduces three important changes: the constant planetary radius a is replaced by the local radial distance $r = a + z$, the constant gravity G becomes altitude-dependent $g(r)$, and the full Coriolis and spherical curvature terms are retained in the momentum equations. The resulting GMCORE governing equations are written as follows:

$$\frac{\partial \mathbf{V}}{\partial t} = -\xi_a \mathbf{k} \times \mathbf{V} - \nabla_\eta^d K - \dot{\eta}\frac{\partial \mathbf{V}}{\partial \eta} - \frac{\rho_d}{\rho}\left(\frac{1}{\rho_d}\nabla_\eta^d p + \frac{\partial p}{\partial \pi}\nabla_\eta^d \phi\right) - 2\Omega\cos\varphi\, w\mathbf{i} - \frac{w}{r}\mathbf{V} + F_V \tag{1}$$

$$\frac{\partial w}{\partial t} = -\mathbf{V}\cdot\nabla_\eta^d w - \dot{\eta}\frac{\partial w}{\partial \eta} - g(r) + \frac{\rho_d}{\rho}G\left(\frac{r}{a}\right)^2\frac{\partial p}{\partial \pi} + 2\Omega\cos\varphi\, u + \frac{u^2+v^2}{r} + F_w \tag{2}$$

$$\frac{\partial}{\partial t}\left(\frac{\partial \pi}{\partial \eta}\right) = -\nabla_\eta^d\cdot\left(\frac{\partial \pi}{\partial \eta}\mathbf{V}\right) - \frac{\partial}{\partial \eta}\left(\frac{\partial \pi}{\partial \eta}\dot{\eta}\right) \tag{3}$$

$$\frac{\partial}{\partial t}\left(\frac{\partial \pi}{\partial \eta}\theta_m\right) = -\nabla_\eta^d\cdot\left(\frac{\partial \pi}{\partial \eta}\mathbf{V}\theta_m\right) - \frac{\partial}{\partial \eta}\left(\frac{\partial \pi}{\partial \eta}\dot{\eta}\theta_m\right) + F_{\theta_m} \tag{4}$$

$$\frac{\partial}{\partial t}\left(\frac{\partial \pi}{\partial \eta}q_i\right) = -\nabla_\eta^d\cdot\left(\frac{\partial \pi}{\partial \eta}\mathbf{V}q_i\right) - \frac{\partial}{\partial \eta}\left(\frac{\partial \pi}{\partial \eta}\dot{\eta}q_i\right) + F_{q_i},\ i = 1,\ldots,N \tag{6}$$

$$\frac{\partial \phi}{\partial t} = -\mathbf{V}\cdot\nabla_\eta^d\phi - \dot{\eta}\frac{\partial \phi}{\partial \eta} + wg(r) + F_\phi \tag{7}$$

where $\mathbf{V} = (u\mathbf{i}, v\mathbf{j})$ is the wind vector, $\dot{\eta}$ is the vertical coordinate velocity, ∇_η^d is the deep-atmosphere horizontal operator, $K = (u^2+v^2)/2$ is the horizontal kinetic energy, π is the hydrostatic dry air mass, Ω is the angular rotation rate of planetary, ρ_d and ρ denote the dry air and total density, ϕ is the geopotential and F represents the unresolved physical tendencies. The deep-atmosphere absolute vorticity ξ_a is correspondingly written as

$$\xi_a = f + \frac{1}{r^2\cos\varphi}\left[\frac{\partial(rv)}{\partial\lambda} - \frac{\partial(ru\cos\varphi)}{\partial\varphi}\right] \tag{8}$$

https://doi.org/10.5194/egusphere-2026-2297
Preprint. Discussion started: 5 June 2026

The layer-averaged mass continuity and thermodynamic equations are then expressed in conservative form as

$$\frac{\partial}{\partial t}(\delta\pi) = -\nabla_\eta^d \cdot (\delta\pi \mathbf{V}) - \delta\left(\frac{\partial \pi}{\partial \eta}\dot{\eta}\right) \tag{9}$$

$$\frac{\partial}{\partial t}(\delta\pi\theta_m) = -\nabla_\eta^d \cdot (\delta\pi \mathbf{V}\theta_m) - \delta\left(\frac{\partial \pi}{\partial \eta}\dot{\eta}\theta_m\right) + F_{\theta_m} \tag{10}$$

where θ_m is the modified potential temperature including the thermodynamic effects of moisture species (Yessad and Wedi, 2011; Lauritzen et al., 2018). In this form it is already evident that the deep-atmosphere extension changes not only the explicit dynamical terms, such as $g(r)$ and the curvature contributions, but also the geometric structure of the transport operators that must be discretized.

For the numerical discretization, the operator modifications follow naturally from the replacement of the constant radius by the local radial distance on the generalized η-surfaces. The horizontal gradient and pseudo-horizontal divergence therefore become

$$\nabla_\eta^d \alpha = \frac{1}{a\cos\varphi}\frac{a}{r}\frac{\partial \alpha}{\partial \lambda}\mathbf{i} + \frac{1}{a}\frac{a}{r}\frac{\partial \alpha}{\partial \varphi}\mathbf{j} \tag{11}$$

$$\nabla_\eta^d \cdot \mathbf{B} \equiv \frac{1}{a\cos\phi}\left(\frac{\partial}{\partial \lambda}\left(\frac{a}{r}B_\lambda\right) + \frac{\partial}{\partial \phi}\left(\frac{a}{r}\cos\phi\, B_\phi\right)\right) \tag{12}$$

where α and $\mathbf{B}$ are arbitrary scalar and vector. Here the factor a/r is part of the local horizontal metric on the η-surface. It cannot, in general, be treated as a purely layer-dependent multiplicative factor, because the terrain-following η-surface may still carry horizontal variations of r. Consequently, the deep metric does not generally commute with the horizontal derivatives, and the metric factor must remain attached to the face fluxes or, equivalently, inside the deep divergence operator used by the discrete scheme.

It is also necessary to distinguish the pseudo-horizontal divergence appearing in the transport operators from the true three-dimensional divergence D_3 of the velocity field. Following Wood and Staniforth (2003), the exact relationship is

$$D_3 = \nabla_r^d \cdot \boldsymbol{V} + \frac{\partial w}{\partial r} + \frac{2w}{r} \tag{13}$$

In the continuous equations, the factor $1/r$ may be understood either as part of the modified horizontal mass flux or as part of the deep horizontal divergence operator (Wood and Staniforth, 2003). These two understandings are equivalent only when the metric factor remains inside the horizontal derivative and is evaluated at the same face location as the flux. For the GMCORE mass-based discretization, this means that the local radius must be diagnosed and interpolated consistently to the staggered positions required by the horizontal mass flux, pressure-gradient force and advection process.

The vertical transport operator requires a different geometric correction. Because the upper and lower interfaces of a control volume lie on spherical shells of different radii, the vertical mass and tracer fluxes must be weighted by the shell-area factor $(r/a)^2$ before calculating the vertical flux divergence. This shell-area weighting belongs specifically to the vertical transport, whereas the horizontal transport is controlled by the local edge modification and the deep version horizontal divergence on the

https://doi.org/10.5194/egusphere-2026-2297
Preprint. Discussion started: 5 June 2026

staggered grids. It is crucial for both conservation and numerical stability to consistently use appropriate and consistent discrete deep-atmosphere geometric extensions in calculations involving pressure gradients, horizontal divergence, vertical flux divergence, and advection.

2.2. Mass-based hybrid vertical coordinate

We use the dry mass terrain-following vertical coordinate (Kasahara, 1974; Simmons and Burridge, 1981), denoted as η. As demonstrated by Wood and Staniforth (2003), a mass-based vertical coordinate requires adjustment for the deep-atmosphere. In contrast to Laprise (1992), the deep-atmosphere mass coordinate chooses $\rho r^2 \frac{\partial r}{\partial s}$ as a constant instead of $\rho a^2 \frac{\partial r}{\partial s}$. This makes the definition of hydrostatic pressure coordinate turn to a more physical description of the atmosphere mass above a cell.

An obvious difference in this deep-atmosphere mass-coordinate dycore is the diagnostic calculation of the radial distance r. In the η-coordinate, to determine the radial distance r without relying on complex iterative solvers, GMCORE directly integrates the exact hydrostatic differential equation. The deep-atmosphere hydrostatic relation is given by:

$$\frac{\partial \pi}{\partial \eta} = -\rho g_0 \left(\frac{r}{a}\right)^2 \frac{\partial r}{\partial \eta} \tag{14}$$

By rearranging the terms to isolate the geometric dependence, we obtain:

$$r^2 \frac{\partial r}{\partial \eta} = -\frac{a^2}{\rho g_0} \frac{\partial \pi}{\partial \eta} \tag{15}$$

Recognizing the exact differential form $r^2\,\partial r = \frac{1}{3}\partial(r^3)$, this relation can be analytically integrated from the planetary surface (where $r = r_s$ and $\pi = \pi_s$) upwards to any given model level k:

$$r_k^3 - r_s^3 = \frac{3a^2}{g_0} \int_{\pi_k}^{\pi_s} \frac{1}{\rho} d\pi \tag{16}$$

In the numerical implementation of the dynamical core, this integral is evaluated layer-by-layer from the surface upward. Let $\Delta\pi$ represents the hydrostatic pressure depth of a layer, which is directly linked to the layer mass Δm. The radial distance $r_{k+\frac{1}{2}}$ at a specific half model level is diagnosed through a discrete cumulative summation of the density-weighted layers:

$$r_{k+\frac{1}{2}} = \left(r_s^3 + \frac{3a^2}{g_0} \sum_{l=k}^{k_{sfc}} \frac{\Delta \pi_k}{\bar{\rho}_l} \right)^{1/3} \tag{17}$$

where $\Delta\pi_k = \pi_{k+\frac{1}{2}} - \pi_{k-\frac{1}{2}}$ is the dry-air weight between two-layer interfaces, the $\bar{\rho}_l$ is the density at the layer center (evaluated at full level).

Furthermore, the choice of a dry mass terrain-following coordinate offers advantages for coupling the dycore with physical parameterizations. Because the vertical coordinate inherently dictates the atmosphere mass above each model level, the calculation of optical depth for shortwave radiation becomes straightforward and direct. This bypasses the complex density-

https://doi.org/10.5194/egusphere-2026-2297
Preprint. Discussion started: 5 June 2026

height conversions required in purely geometric height-based models, significantly enhancing the thermodynamic consistency of short-wave heating (Borchert et al., 2019).

2.3. Spatial discretization and grid staggering

In practical numerical implementation, the discrete spatial discretization must strictly matches the grid geometry expansion. In shallow-atmosphere dycore, the horizontal grid cell area is assumed constant throughout all vertical levels. On the contrast, in the deep-atmosphere dycore, the discrete finite-volume cell area $A(r)$ and grid edge lengths $\Delta l(r)$ physically change as the altitude increases. Following the illustration and discretization shown in Borchert et al. (2019) and Skamarock et al. (2021), GMCORE explicitly incorporates this radial scaling into its spatial operators. Specifically, the cell area and edge lengths at a given radial distance r are scaled by geometric factors of $(r/a)^2$ and (r/a), respectively, relative to their reference values at the planetary surface a.This guarantees the conservation of total atmosphere mass and systematically helps prevent the spurious generation of global angular momentum.

GMCORE utilizes a regular latitude-longitude grid organized on an Arakawa C-grid staggering. This staggering optimally represents inertia-gravity wave dispersion characteristics and suppresses computational mode. For advection process, GMCORE employs a modified flux-form semi-Lagrangian (FFSL) advection scheme SWIFT with a third-order polynomial reconstruction and flux limiters, to enable large advection time step size and maintain the monotonicity of tracers (Lin and Rood, 1996; Bendall and Kent, 2025).

A challenge for latitude-longitude grids is the severe convergence of meridians at the poles, which typically induces numerical noise and structural deformation in cross-polar flows. To circumvent this singularity, GMCORE redefines the relative vorticity around the poles via Stokes' theorem (Li et al., 2020). This specific physical constraint governs the evolution of potential enstrophy, effectively suppressing artificial computational noise sources precisely at the polar singularities.

2.4. Time integration: semi-implicit scheme

To circumvent the Courant-Friedrichs-Lewy (CFL) stability limits imposed by vertically propagating acoustic waves, GMCORE employs a semi-implicit (SI) time-integration scheme. Following the vertical implicit treatment used in nonhydrostatic models GRIST (Zhang et al., 2019) and ICON (e.g., Zängl et al., 2015), the prognostic variables are computed directly as full-field quantities without relying on a stationary, global background reference profile.

In this semi-implicit formulation, horizontal advection, vertical advection, the full Coriolis force and subgrid physical tendencies are evaluated explicitly. Conversely, the terms responsible for high-frequency vertical acoustic wave propagation—specifically the vertical pressure gradient force in the vertical momentum equation, and the associated $w \cdot g(r)$ term in the geopotential equation—are treated implicitly. By introducing an off-centering weight $\alpha \in [0.5,1.0]$, the implicit equations for the vertical velocity w and the geopotential ϕ can be conceptually simplified as:

$$w^{n+1} = \Delta t \cdot \mathcal{R}_w^n + \alpha \Delta t L g \left(\frac{\delta p}{\delta \pi}\right)^{n+1} \tag{18}$$

https://doi.org/10.5194/egusphere-2026-2297
Preprint. Discussion started: 5 June 2026

$$\phi^{n+1} = \Delta t \cdot \mathcal{R}_{\phi}^{n} + \alpha \Delta t g w^{n+1} \tag{19}$$

where $\mathcal{R}_{w}^{n}$ and $\mathcal{R}_{\phi}^{n}$ represent the total explicit residual tendencies evaluated at time step n, $L = \frac{\rho_d}{\rho} = \frac{1}{1+q_m}$ is the moist contribution. The increment of pressure δp is diagnostically linked to $\delta\phi$ and the thermodynamic properties through the equation of state:

$$\frac{p^{n+1} - p^n}{p^n} \approx \gamma \left(\frac{(\delta \pi \theta_m)^{n+1}}{(\delta \pi \theta_m)^n} - \frac{\delta \phi^{n+1}}{\delta \phi^n} \right) \tag{20}$$

By substituting the implicit increments of geopotential ($\delta\phi$) and pressure (δp) into the discretized vertical momentum equation, we eliminate the dependencies on other prognostic variables. This procedure reduces the coupled equations into a one-dimensional vertical equation for the vertical velocity w within each independent grid column. When discretized on the vertically staggered levels, it directly forms a standard tri-diagonal linear system:

$$A_{k-\frac{1}{2}} w_{k-\frac{1}{2}} + B_{k+\frac{1}{2}} w_{k+\frac{1}{2}} + C_{k+\frac{3}{2}} w_{k+\frac{3}{2}} = \widetilde{R_{w,k+\frac{1}{2}}} \tag{21}$$

where $\widetilde{R_{w,k+\frac{1}{2}}}$ includes all the explicitly resolved forcing terms. The matrix coefficients $A_{k-\frac{1}{2}}, B_{k+\frac{1}{2}}$, and $C_{k+\frac{3}{2}}$ are dynamically updated at each time step based on the local atmospheric state.

This one-dimensional tri-diagonal system is solved independently for every vertical column using the highly efficient Thomas algorithm, demanding no horizontal communication. Once the vertical velocity w is obtained, the increments for the remaining implicitly treated variables (such as $\delta\phi$ and δp) are sequentially back-substituted. This semi-implicit vertical nonhydrostatic solver successfully decouples the fast vertical acoustic wave speeds from the integration stability criteria. This approach allows GMCORE to avoid solving global elliptic equations during nonhydrostatic calculations and to increase the time step.

2.5. Polar filtering and damping

Due to the convergence of the latitude and longitude grids at the poles, the zonal grid spacing shrinks significantly in the polar regions. As a result, the local zonal CFL number increases sharply in the polar region and can impose a severe stability constraint on the explicit part of the dynamical time integration.

In GMCORE, we apply an adaptive zonal Gaussian convolution filter for dynamical tendencies along each latitude circle. For an arbitrary tendency field $\mathcal{M}$ in u, v, θ_m, π_s and advection tendency of w, ϕ, the filtered field $\mathcal{M}^{filt}$ can be written

$$\mathcal{M}_{i,j,k}^{filt} = \sum_{m=-H_j}^{H_j} w_{j,m} \mathcal{M}_{i+m,j,k}\,, \tag{22}$$

where $w_{j,m}$ is the Gaussian weight at offset m on the j-th latitude circle, and H_j is the corresponding half-width of the stencil. Because the zonal direction is periodic, the index $i + m$ is wrapped cyclically around the latitude circle.

The kernel width is not prescribed as a constant, but diagnosed adaptively from the local zonal stability constraint. In the implementation, a dimensionless width parameter is first defined as

https://doi.org/10.5194/egusphere-2026-2297
Preprint. Discussion started: 5 June 2026

$$W_j = \alpha_f \frac{c_f \Delta t}{\Delta x_j} \tag{23}$$

where Δx_j is the zonal grid spacing on latitude ϕ_j, Δt is the dynamical time step, and c_f is a characteristic filtering wave speed now set to 300 m s^{-1}. The coefficient α_f is the parameter controlling the overall filter strength. The factor $\frac{c_f \Delta t}{\Delta x_j}$ has the form of a zonal CFL number, so that the filter automatically becomes stronger where the grid is more restrictive. This latitude-dependent feature provides a smooth transition of the kernel width with latitude and helps avoid abrupt changes in filtering strength.

The continuous kernel is represented on the discrete stencil through a Gaussian profile. For a stencil of width $N_j = 2H_j + 1$, the unnormalized weights are defined by

$$\widetilde{w}_{j,m} = \frac{1}{s_j \sqrt{2\pi}} \exp\left(-\frac{m^2}{2s_j^2}\right), m = -H_j, \ldots, H_j \tag{24}$$

with $s_j = \frac{W_j}{\sigma_f}$, where σ_f is a prescribed shape parameter controlling the relation between the diagnosed width W_j and the standard deviation of the discrete Gaussian kernel. The final filter weights are then normalized as

$$w_{j,m} = \widetilde{w}_{j,m} \Big/ \sum_{m=-H_j}^{H_j} \widetilde{w}_{j,m}, \sum_{m=-H_j}^{H_j} w_{j,m} = 1 \tag{25}$$

The normalization procedure guarantees that the filter preserves constant fields. In this way, the filter automatically strengthens near the poles while remaining weak in lower latitudes. Because the method uses only finite-width local convolution, it avoids the global communication required by FFT-based polar filtering and is therefore well suited to parallel latitude–longitude grid implementations.

In addition to the polar Gaussian filter, GMCORE applies optional horizontal divergence damping to the momentum field (Lauritzen et al., 2011). This damping is to diffuse the divergent part of flow noise that may otherwise accumulate near steep gradients, in the upper levels, or in the polar region. The damping is formulated in terms of the horizontal divergence, let

$$\delta_h = \nabla_h \cdot \boldsymbol{v_h} \tag{26}$$

where $\boldsymbol{v_h} = (u, v)$ is the wind vector. δ_h is the divergence. The second-order divergence damping is written as

$$\left.\frac{\partial \boldsymbol{v_h}}{\partial t}\right|_{\delta,2} = \nu_{\delta,2} \nabla_h \delta_h \tag{27}$$

and a more scale-selective fourth-order option is

$$\left.\frac{\partial \boldsymbol{v_h}}{\partial t}\right|_{\delta,4} = -\nu_{\delta,4} \nabla_h \nabla_h^2 \delta_h \tag{28}$$

The damping coefficients $\nu_{\delta,2}$ and $\nu_{\delta,4}$ are scaled with the local grid area and time step and can be smoothly enhanced near the poles or upper levels.

https://doi.org/10.5194/egusphere-2026-2297
Preprint. Discussion started: 5 June 2026

$$\nu_{\delta,2} \sim C_2 \frac{A}{\Delta t}, \qquad \nu_{\delta,4} \sim C_4 \frac{A^2}{\Delta t} \tag{29}$$

3. Test cases and simulation results

To test the validity and performance of deep-atmosphere version of GMCORE, particularly the deep-atmosphere modifications described in Section 2, two standard idealized test cases are selected.

3.1. Deep-atmosphere baroclinic wave

The idealized baroclinic wave test case evaluates the model's ability to simulate mid-latitude baroclinic processes. Following the model parameters proposed by Ullrich et al. (2014), we employ this test to demonstrate the characteristics of the deep-atmosphere configurations.

The initial conditions feature a mid-latitude jet in hydrostatic and geostrophic balance (Staniforth and White, 2012), which is subsequently perturbed to trigger baroclinic instability. Simulations are conducted using both the deep-atmosphere and the shallow-atmosphere solvers.

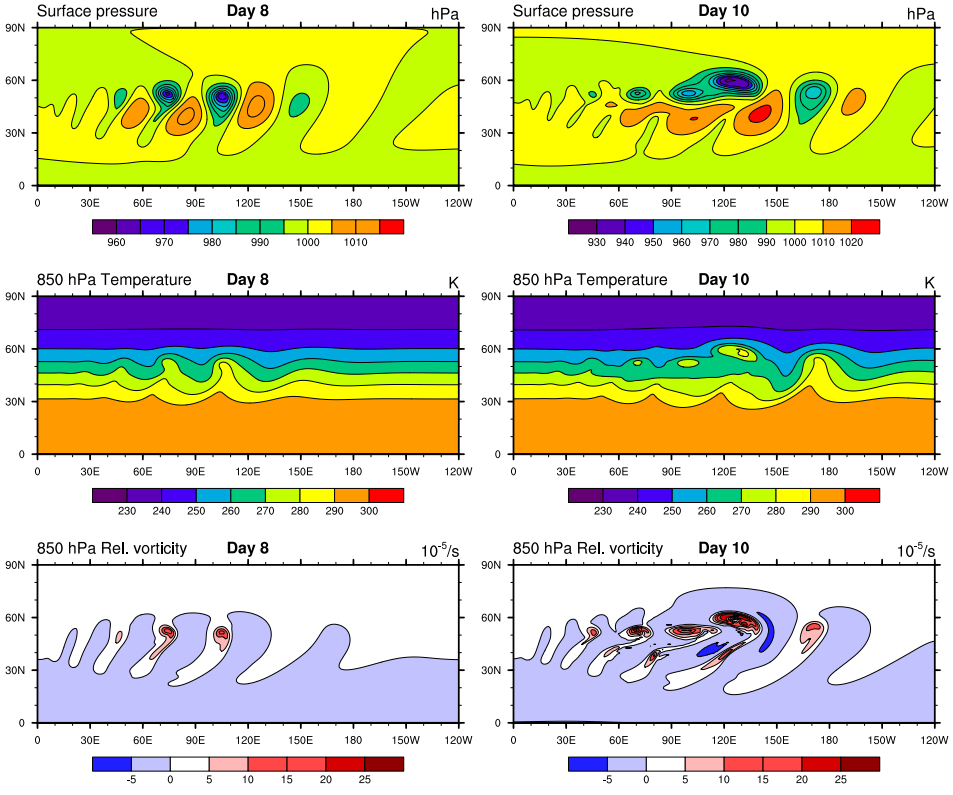

Figure 1: Evolution of the surface pressure, 850 hPa temperature and relative vorticity for the deep baroclinic wave test at days 8 and 10.

https://doi.org/10.5194/egusphere-2026-2297
Preprint. Discussion started: 5 June 2026

Figure 1 shows the evolution of surface pressure, 850 hPa temperature, and 850 hPa relative vorticity in the deep configuration at days 8 and 10. The developing wave exhibits the familiar life cycle of baroclinic instability: a midlatitude disturbance grows along the jet, amplifies downstream, and evolves into a mature cyclone–anticyclone structure. Overall, the simulated fields are consistent with the standard behaviour reported in previous model intercomparisons of this test case (Ullrich et al., 2014; Wood et al., 2014; Borchert et al, 2019; Skamarock et al, 2021; Kelly et al., 2026; Yatunin et al., 2026), and indicate that the GMCORE deep-atmosphere dycore is able to maintain the balanced basic state and reproduce the expected evolution of the wave under Earth-like conditions.

In a standard Earth-radius configuration ($a \approx 6371$ km), the troposphere is extremely thin relative to the planet's radius. Consequently, the deep-atmosphere geometrical scaling $(r/a)^2$ and the variable gravity $g(r)$ introduce very small dynamical differences compared to the shallow-atmosphere.

To amplify the dynamical differences between the deep- and shallow-atmosphere equations, we follow Ullrich et al. (2014) and employ the reduced-radius, or "small-Earth", baroclinic-wave experiment, in which the planetary radius is decreased by a factor of 20 while the rotation rate is increased by the same factor. Under the standard Earth-radius configuration, the two configurations produce nearly indistinguishable baroclinic-wave evolutions, whereas in the X20 configuration the shallow-atmosphere assumption is no longer strictly valid and the two solutions separate much more clearly.

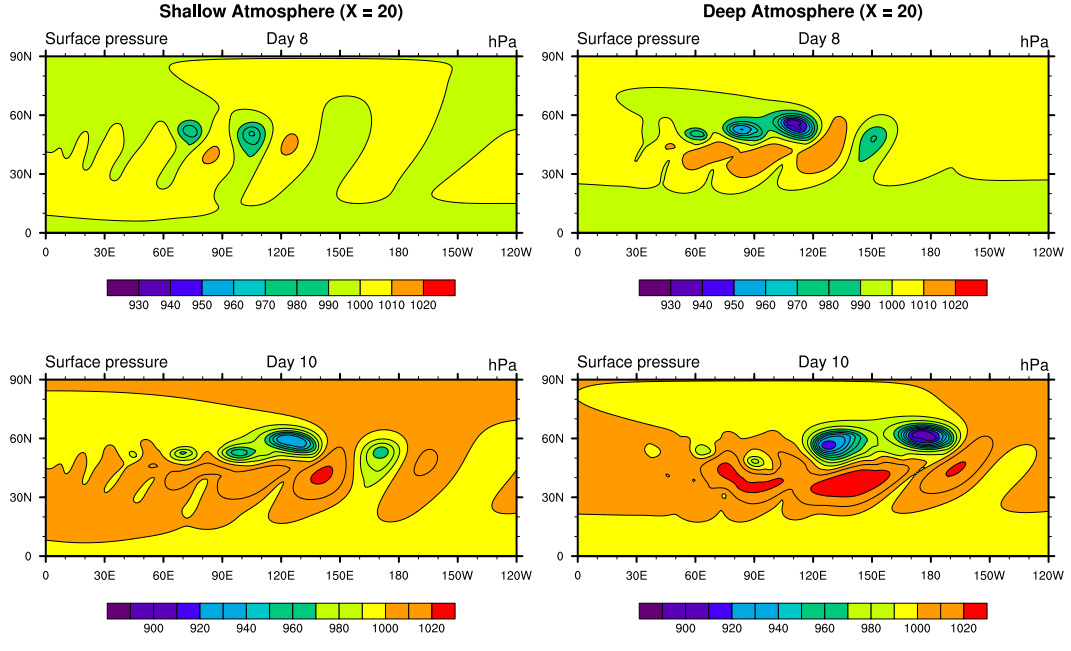

Figure 2: Surface pressure fields in the X20 reduced-radius baroclinic-wave experiment for the shallow-atmosphere and deep-atmosphere configurations at days 8 and 10. Following Ullrich et al. (2014), the planetary radius is reduced by a factor of 20 and the rotation rate is increased by the same factor in order to exaggerate the differences between the two equation sets.

https://doi.org/10.5194/egusphere-2026-2297
Preprint. Discussion started: 5 June 2026

In our X20 simulations, the shallow-atmosphere solution retains a comparatively weaker and smoother baroclinic-wave structure, broadly consistent with the reference behaviour reported by Ullrich et al. (2014). In contrast, the deep-atmosphere solution exhibits a more rapid amplification of the wave and a substantially stronger cyclonic development. By day 8, the deep-atmosphere field already shows a more compact and intense low-pressure center together with a more amplified downstream wave; by day 10, the contrast becomes even more pronounced, with the deep-atmosphere solution characterized by a deeper and stronger mature cyclone, while the shallow-atmosphere counterpart remains less developed. This behaviour is consistent with Ullrich et al. (2014), who showed that in the X20 experiment the deep-atmosphere integration intensifies much more rapidly and drives the minimum surface pressure below 900 hPa by day 10, whereas the shallow-atmosphere result remains much closer to the standard baroclinic-wave evolution.

To sum up, in the reduced-radius baroclinic-wave experiment, GMCORE reproduces the pronounced separation between the deep- and shallow-atmosphere solutions reported in earlier studies. This performance is consistent with the purpose of the small-Earth configuration proposed by Ullrich et al. (2014), namely to exaggerate the differences between the two equation sets once the shallow-atmosphere assumption is no longer strictly valid. At the same time, we note that the interpretation of this test case remains non-trivial. As discussed by Skamarock et al. (2021), a substantial part of the previously reported deep–shallow differences in the X20 case may arise from differences in the analytic initial states, rather than directly from the temporal integration of the deep versus shallow equations themselves. For this reason, we regard the X20 experiment primarily as a benchmark-reproduction test. Its main value in the present study is to demonstrate that the deep-atmosphere extension of GMCORE is able to recover the canonical numerical behaviour documented in the literature, thereby providing confidence in the correctness of the model equation and implementation.

3.2. Tropical cyclone simulation

Next, we try to use an idealized tropical cyclone (TC) test case, which was proposed by Reed and Jablonowski (2011). In this case, an initial warm-core vortex that satisfies gradient wind balance is inserted in an aquaplanet without topography. This configuration eliminates the land surfaces and the real environmental flow effects, making it an ideal test-bed for isolating and evaluating the deep-atmosphere modification. More precisely, due to the low model top (about 20km) of this case, geometric and variable-gravity effects are expected to be much smaller than the retained nontraditional Coriolis contribution. This case is therefore used mainly to examine the impact of the NCTs-related deep-atmosphere terms.

We follow the standard parameters and run this case at a horizontal resolution of 0.25° and 0. 125° for 10 days. To isolate the dynamical impact of the deep-atmosphere terms, the experiment is executed using both the nonhydrostatic deep-atmosphere (NHD) and nonhydrostatic shallow-atmosphere (NHS) configurations.

https://doi.org/10.5194/egusphere-2026-2297
Preprint. Discussion started: 5 June 2026

3.2.1 Tropical cyclone trajectories comparison

During the dynamical evolution of a tropical cyclone, the full three-dimensional Coriolis force—specifically the NCTs—is conventionally neglected in traditional shallow-atmosphere models. However, in the deep tropics where $\cos\varphi$ approaches its maximum, and within the TC eyewall region characterized by exceptionally strong vertical updrafts (with w frequently exceeding 10 m s^{-1}), the horizontal and vertical momentum forcings generated by the NCT become non-negligible in magnitude. Although previous idealized cloud-resolving studies (e.g., Igel and Biello, 2020) have highlighted the potential impact of NCT on equatorial convection, the macroscopic dynamical effects of this mechanism within a global deep-atmosphere dycore during a complete TC life cycle remain largely unverified.

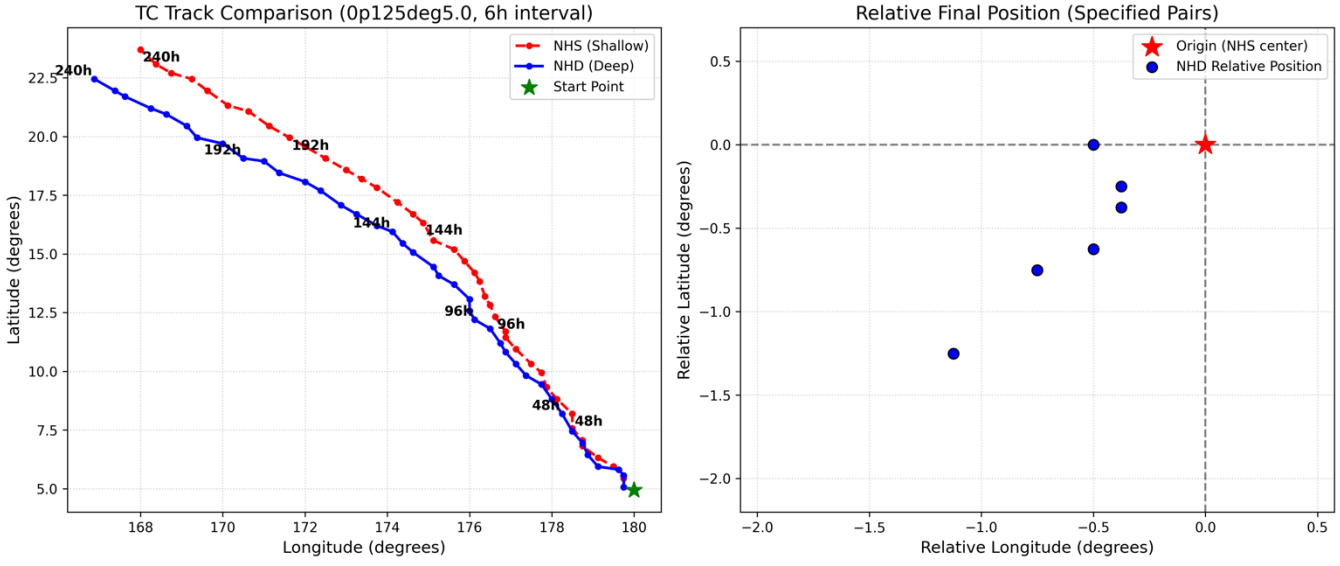

Figure 3: Simulated tropical cyclone trajectories for the nonhydrostatic shallow-atmosphere (NHS, red line) and deep-atmosphere (NHD, blue line) configurations at a horizontal resolution of 0.125°. Over the integration period, the perturbation center propagates north-westward and the initial perturbation latitude is set at 5°N, showing on left panel. For right panel, all NHS TC center at final timestep set to (0,0), the blue points represent the relative positions of all 0.125° and 0.25° experiments with different perturbation latitudes.

As shown in Fig. 3, both NHS and NHD simulations produce a north-westward-moving tropical cyclone, but the NHD trajectory exhibits a systematic south-westward displacement relative to the NHS trajectory as the vortex develops. This result is qualitatively similar to that reported by Liang and Chan (2005), who found that inclusion of the $2\Omega\cos\varphi\, w$ term had little effect on tropical-cyclone intensity but led to a westward to south-westward trajectory deviation. We also test different perturbations at different latitudes and get the same conclusion (Fig. 3b).

In our results, both simulations remain similar in terms of storm intensity and axisymmetric structure. As already indicated in the present supplementary, the two simulations show no essential difference in the minimum central pressure, maximum low-

https://doi.org/10.5194/egusphere-2026-2297
Preprint. Discussion started: 5 June 2026

level wind speed, or the warm-core structure, suggesting that the leading-order thermodynamic processes controlling storm intensification are not strongly altered by the deep-atmosphere extension.

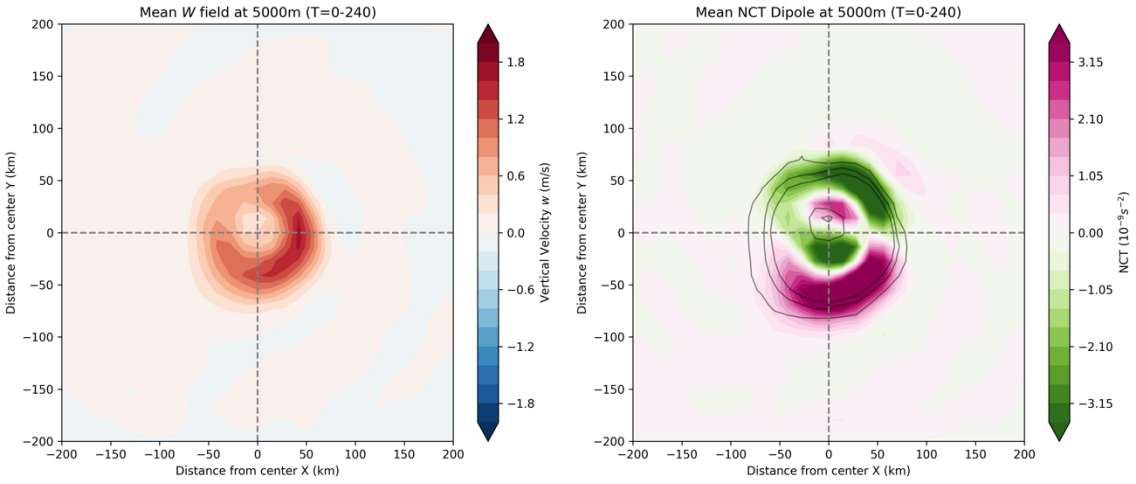

Figure 4: Horizontal cross-sections of time-averaged (T = 0–240h) atmospheric variables at an altitude of 5000 m. **(Left)** Mean vertical velocity (w) field (m/s), illustrating a core of intense upward motion centered at the origin, surrounded by weaker spiral rainband structures. **(Right)** Mean NCTs dipole (10^{-9} s^{-2}), showing a distinct positive (green) and negative (pink) coupled structure near the vortex core. Both panels are centered on the system's axis, with distances indicated in kilometers from the center (X, Y).

To interpret this trajectory difference, Figure 4 shows the time-mean horizontal structure at 5 km altitude. In Fig. 4a, the mean vertical velocity field exhibits a compact core of strong ascent near the storm center, surrounded by weaker spiral rainband structures. This indicates that the mature vortex maintains a well-defined eyewall-like updraft region. Closely collocated with this convective core, in Fig. 4b, we show the quantity

$$\Gamma = 2\Omega \cos\phi \frac{\partial w}{\partial y} \tag{30}$$

which represents the vorticity tendency associated with the NCTs in the x-momentum equation. Here, the dipole-like structure refers to the pair of opposite-signed Γ anomalies on the two sides of the storm center. In other words, the meridional gradient of the eyewall vertical motion produces a positive tendency on one side of the core and a negative tendency on the other, giving rise to an organized inner-core asymmetry rather than an axisymmetric distribution.

https://doi.org/10.5194/egusphere-2026-2297
Preprint. Discussion started: 5 June 2026

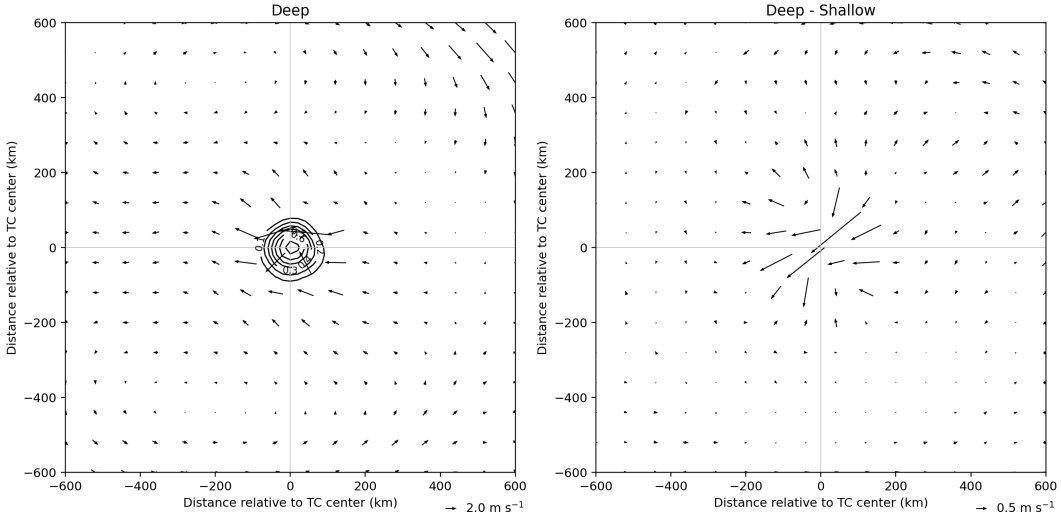

Figure 5: Horizontal wind velocity vectors and vertical velocity contours at an altitude of 1500 m. **(Left)** "Deep" case wind field, showing a cyclonic circulation with a localized maximum in wind speed (contours, m/s) near the Tropical Cyclone (TC) center. Reference vector indicates a magnitude of 2.0 m s^{-1}. **(Right)** Difference in wind velocity between the "Deep" and "Shallow" cases (Deep – Shallow). This panel highlights the variation in environmental flow and the intensity of the low-level circulation between the two experiments, with a reference vector of 0.5 m s^{-1}. All coordinates are relative to the TC center (km).

This dipole is dynamically consistent with the near-core easterly anomaly shown in Fig. 5, which in turn is consistent with the south-westward displacement of the NHD trajectory. Figure 5 shows the horizontal winds at 1.5 km. The left panel gives the circulation in the NHD run, and the right panel shows the wind difference between the deep and shallow simulations. The main feature in the difference field is an easterly anomaly near the storm center. This anomaly is important because it is consistent with the south-westward displacement of the NHD trajectory in Fig. 3. In the Liang and Chan (2005) experiments, the additional Coriolis term associated with vertical motion produced a generally easterly flow near the TC center, and this easterly flow was identified as the immediate cause of the westward or south-westward displacement. Our result is not identical to their diagnosis, but the low-level easterly anomaly in Fig. 5 points in the same direction. It suggests that the south-westward shift in the NHD trajectory is tied to a coherent change in the inner-core flow rather than to random differences accumulated during the integration.

At the same time, the present analysis remains more limited than that in Liang and Chan (2005). We have not yet constructed a full asymmetric wind composite like their Fig. 7, so the phase relationship among eyewall ascent, vorticity tendency, and asymmetric gyres is not shown explicitly here. For this reason, the mechanism discussed above should be taken as an interpretation of the present results rather than as a complete dynamical proof. The result from this test is simpler: the GMCORE deep-atmosphere dycore gives a TC evolution that is similar to the shallow-atmosphere run in intensity, but different in trajectory, and this trajectory difference is accompanied by an organized inner-core asymmetry and a low-level easterly anomaly in the deep-minus-shallow wind field.

https://doi.org/10.5194/egusphere-2026-2297
Preprint. Discussion started: 5 June 2026

In summary, by strictly retaining the complete $2\Omega\cos\varphi$ dynamical terms, the GMCORE deep-atmosphere dynamical core successfully captures the asymmetric outflow mechanism excited by intense convective vertical motions, reasonably reproducing the south-westward deflection of the TC trajectory. This further verifies the physical fidelity and necessity of the nonhydrostatic deep-atmosphere dycore for high-resolution simulations of extreme weather events.

Existing studies have documented tropical-cyclone trajectory errors characterized by premature recurvature and north/eastward displacement, often linked directly to biases in the environmental steering flow. Meanwhile, deep-atmosphere and NCTs studies suggest that the omitted $2\Omega cos\phi$ terms can systematically modify tropical convective asymmetries and cyclone motion. Therefore, neglect of these terms may represent a dynamically plausible, but not yet conclusively established, contributor to such trajectory biases.

4. Conclusions

In this study, we implemented an extension for the deep-atmosphere within a nonhydrostatic dynamical core (GMCORE) and validated the dycore's performance through numerical simulations of ideal baroclinic waves and tropical cyclones. The new version of GMCORE extends the original shallow-atmosphere equations to the deep-atmosphere ones, retaining the full three-dimensional Coriolis force and variable gravity terms, and incorporating spherical geometry-related terms. A key feature of this extension is the adoption of a generalized dry terrain-following mass-based coordinate system and the use of the Wood and Staniforth (2003) diagnostic formula for the distance from the Earth's center. This ensures that the structural form of the deep-atmosphere hydrostatic relations remains consistent with that of the shallow-atmosphere formulation, while retaining the advantages of the original solver. In this way, GMCORE has evolved from its original nonhydrostatic framework into a dycore that supports deep-atmosphere nonhydrostatic dynamics.

The extension was evaluated using two standard idealized test cases. In the deep baroclinic wave test, the deep- and shallow-atmosphere solutions remain close under the standard Earth-radius configuration, as expected when the atmospheric depth is still small relative to the planetary radius. In the reduced-radius X20 configuration, however, the two solutions separate clearly, and the deep-atmosphere version GMCORE reproduces the deep–shallow differences reported in previous studies. We therefore regard this test as a correctness-oriented benchmark, to check the new equation set and its numerical implementation.

The tropical cyclone case highlights a different aspect of the deep-atmosphere extension. In this low-latitude, strongly rotating, vertically active regime, the deep-atmosphere effect is therefore associated with the retained NCTs, the terms proportional to $2\Omega\cos\phi$, which couple vertical and horizontal motion in the tropical vortex core. It produces a systematic south-westward trajectory shift relative to the shallow-atmosphere configuration. This difference is accompanied by an inner-core asymmetry and a low-level easterly anomaly in the deep-minus-shallow wind field. The result suggests that the retained NCTs can influence the evolution of weather-scale vortices even when the model top is not especially high and the geometric part of the deep-atmosphere correction remains comparatively weak.

https://doi.org/10.5194/egusphere-2026-2297
Preprint. Discussion started: 5 June 2026

Several limitations should be kept in mind. The X20 baroclinic-wave case is useful for verification, but not ideal for attributing deep–shallow differences purely to the time integration of the two equation sets, because part of the contrast may originate from differences in the analytic initial states. The tropical-cyclone experiment is likewise idealized, and the mechanism linking the track shift to the inner-core asymmetry still requires more systematic diagnosis, including analyses of angular momentum, potential vorticity, and asymmetric circulation. Future work will therefore focus on extending the diagnostics, raising the model top together with appropriate physical parameterizations, and applying the deep-atmosphere GMCORE to problems in tropical dynamics and upper-atmosphere modelling.

Overall, this study demonstrates that GMCORE can be extended from a shallow-atmosphere dycore to a fully compressible deep-atmosphere dycore while retaining the structural advantages of its original mass-based coordinate system and numerical design. In future work, GMCORE will continue to investigate tropical dynamics and the top of the model, while incorporating real physical processes to study the upper atmosphere.

Code and data availability

The deep-atmosphere extension code and scripts are on https://doi.org/10.5281/zenodo.19705647.

Author contributions

The deep-atmosphere extension is a collaboration work between the authors. LD finishes the based nonhydrostatic work and gives the idea of this work. QC finishes the deep-atmosphere programming and test. BW gives the suggestions to some modeling questiones.The authors write this paper.

Competing interests

The authors declare that they have no conflict of interest.

Acknowledgements

This work was supported by the National Natural Science Foundation of China (Grant No.42475135). We also thank for the technical support of the National Large Scientific and Technological Infrastructure "Earth System Numerical Simulation Facility" (https://cstr.cn/31134.02.EL).

Financial support

This research has been supported by the National Natural Science Foundation of China (Grant No.42475135).

https://doi.org/10.5194/egusphere-2026-2297
Preprint. Discussion started: 5 June 2026

References

Akmaev, R. A.: WHOLE ATMOSPHERE MODELING: CONNECTING TERRESTRIAL AND SPACE WEATHER, Reviews of Geophysics, 49, 2011RG000364, https://doi.org/10.1029/2011RG000364, 2011.

Baldwin, M. P. and Dunkerton, T. J.: Stratospheric Harbingers of Anomalous Weather Regimes, Science, 294, 581–584, https://doi.org/10.1126/science.1063315, 2001.

Bendall, T. M. and Kent, J.: SWIFT: A Monotonic, Flux-Form Semi-Lagrangian Tracer Transport Scheme for Flow with Large Courant Numbers, Monthly Weather Review, 153, 565–587, https://doi.org/10.1175/MWR-D-24-0110.1, 2025.

Borchert, S., Zhou, G., Baldauf, M., Schmidt, H., Zängl, G., and Reinert, D.: The upper-atmosphere extension of the ICON general circulation model (version: ua-icon-1.0), Geosci. Model Dev., 12, 3541–3569, https://doi.org/10.5194/gmd-12-3541-2019, 2019.

De Verdière, A. C. and Schopp, R.: Flows in a rotating spherical shell: the equatorial case, J. Fluid Mech., 276, 233–260, https://doi.org/10.1017/S0022112094002545, 1994.

Fritts, D. C. and Alexander, M. J.: Gravity wave dynamics and effects in the middle atmosphere, Reviews of Geophysics, 41, 2001RG000106, https://doi.org/10.1029/2001RG000106, 2003.

Gerkema, T., Zimmerman, J. T. F., Maas, L. R. M., and Van Haren, H.: Geophysical and astrophysical fluid dynamics beyond the traditional approximation, Reviews of Geophysics, 46, 2006RG000220, https://doi.org/10.1029/2006RG000220, 2008.

Gettelman, A., Mills, M. J., Kinnison, D. E., Garcia, R. R., Smith, A. K., Marsh, D. R., Tilmes, S., Vitt, F., Bardeen, C. G., McInerny, J., Liu, H. -L., Solomon, S. C., Polvani, L. M., Emmons, L. K., Lamarque, J. -F., Richter, J. H., Glanville, A. S., Bacmeister, J. T., Phillips, A. S., Neale, R. B., Simpson, I. R., DuVivier, A. K., Hodzic, A., and Randel, W. J.: The Whole Atmosphere Community Climate Model Version 6 (WACCM6), JGR Atmospheres, 124, 12380–12403, https://doi.org/10.1029/2019JD030943, 2019.

Igel, M. R. and Biello, J. A.: The Nontraditional Coriolis Terms and Tropical Convective Clouds, Journal of the Atmospheric Sciences, 77, 3985–3998, https://doi.org/10.1175/JAS-D-20-0024.1, 2020.

Kasahara, A.: Various Vertical Coordinate Systems Used for Numerical Weather Prediction, Mon. Wea. Rev., 102, 509–522, https://doi.org/10.1175/1520-0493(1974)102%253C0509:VVCSUF%253E2.0.CO;2, 1974.

Kelly, J. F., Alves, F. A. V. D. B., Eckermann, S. D., Giraldo, F. X., Reinecke, P. A., and Emmert, J. T.: A nonhydrostatic mass-conserving dynamical core for deep atmospheres of variable composition, Journal of Computational Physics, 552, 114683, https://doi.org/10.1016/j.jcp.2026.114683, 2026.

Kim, Y.-J., Eckermann, S. D., and Chun, H.-Y.: An overview of the past, present and future of gravity-wave drag parametrization for numerical climate and weather prediciton models, Atmos. Ocean, 40, 65–98, https://doi.org/10.3137/ao.410105, 2003.

https://doi.org/10.5194/egusphere-2026-2297
Preprint. Discussion started: 5 June 2026

Laprise, R.: The Euler Equations of Motion with Hydrostatic Pressure as an Independent Variable, Mon. Wea. Rev., 120, 197–207, https://doi.org/10.1175/1520-0493(1992)120%253C0197:TEEOMW%253E2.0.CO;2, 1992.

Lauritzen, P., Jablonowski, C., Taylor, M., and Nair, R. (Eds.): Numerical Techniques for Global Atmospheric Models, Springer Berlin Heidelberg, Berlin, Heidelberg, https://doi.org/10.1007/978-3-642-11640-7, 2011.

Lauritzen, P. H., Nair, R. D., Herrington, A. R., Callaghan, P., Goldhaber, S., Dennis, J. M., Bacmeister, J. T., Eaton, B. E., Zarzycki, C. M., Taylor, M. A., Ullrich, P. A., Dubos, T., Gettelman, A., Neale, R. B., Dobbins, B., Reed, K. A., Hannay, C., Medeiros, B., Benedict, J. J., and Tribbia, J. J.: NCAR Release of CAM-SE in CESM2.0: A Reformulation of the Spectral Element Dynamical Core in Dry-Mass Vertical Coordinates With Comprehensive Treatment of Condensates and Energy, J Adv Model Earth Syst, 10, 1537–1570, https://doi.org/10.1029/2017MS001257, 2018.

Li, J. and Dong, L.: A Long-Time-Step-Permitting Tracer Transport Model on the Regular Latitude–Longitude Grid, Adv. Atmos. Sci., 41, 493–508, https://doi.org/10.1007/s00376-023-2270-z, 2024.

Li, J., Wang, B., and Dong, L.: Analysis of and Solution to the Polar Numerical Noise Within the Shallow-Water Model on the Latitude-Longitude Grid, J Adv Model Earth Syst, 12, e2020MS002047, https://doi.org/10.1029/2020MS002047, 2020.

Liang, X. and Chan, J. C. L.: The Effects of the Full Coriolis Force on the Structure and Motion of a Tropical Cyclone. Part I: Effects due to Vertical Motion, Journal of the Atmospheric Sciences, 62, 3825–3830, https://doi.org/10.1175/JAS3545.1, 2005.

Lin, S.-J. and Rood, R. B.: Multidimensional Flux-Form Semi-Lagrangian Transport Schemes, Mon. Wea. Rev., 124, 2046–2070, https://doi.org/10.1175/1520-0493(1996)124%253C2046:MFFSLT%253E2.0.CO;2, 1996.

Liu, H., Bardeen, C. G., Foster, B. T., Lauritzen, P., Liu, J., Lu, G., Marsh, D. R., Maute, A., McInerney, J. M., Pedatella, N. M., Qian, L., Richmond, A. D., Roble, R. G., Solomon, S. C., Vitt, F. M., and Wang, W.: Development and Validation of the Whole Atmosphere Community Climate Model With Thermosphere and Ionosphere Extension (WACCM-X 2.0), J Adv Model Earth Syst, 10, 381–402, https://doi.org/10.1002/2017MS001232, 2018.

Liu, S., Dong, L., Xi, X., Cheng, X., Liu, J., Pu, Y., Li, Y., Liu, H., Liu, M., Xue, W., Cao, J., and Wang, B.: The Fully Interactive Martian Dust Cycle Simulations by the GoMars Model, Adv. Atmos. Sci., 43, 461–476, https://doi.org/10.1007/s00376-025-5190-2, 2026.

Marshall, J., Hill, C., Perelman, L., and Adcroft, A.: Hydrostatic, quasi-hydrostatic, and nonhydrostatic ocean modeling, J. Geophys. Res., 102, 5733–5752, https://doi.org/10.1029/96JC02776, 1997.

Ong, H. and Roundy, P. E.: Linear effects of nontraditional Coriolis terms on intertropical convergence zone forced large-scale flow, Quart J Royal Meteoro Soc, 145, 2445–2453, https://doi.org/10.1002/qj.3572, 2019.

Phillips, N. A.: The Equations of Motion for a Shallow Rotating Atmosphere and the “Traditional Approximation,” J. Atmos. Sci., 23, 626–628, https://doi.org/10.1175/1520-0469(1966)023%253C0626:TEOMFA%253E2.0.CO;2, 1966.

Reed, K. A. and Jablonowski, C.: An Analytic Vortex Initialization Technique for Idealized Tropical Cyclone Studies in AGCMs, Monthly Weather Review, 139, 689–710, https://doi.org/10.1175/2010MWR3488.1, 2011.

https://doi.org/10.5194/egusphere-2026-2297
Preprint. Discussion started: 5 June 2026

Satoh, M., Matsuno, T., Tomita, H., Miura, H., Nasuno, T., and Iga, S.: Nonhydrostatic icosahedral atmospheric model (NICAM) for global cloud resolving simulations, Journal of Computational Physics, 227, 3486–3514, https://doi.org/10.1016/j.jcp.2007.02.006, 2008.

Simmons, A. J. and Burridge, D. M.: An Energy and Angular-Momentum Conserving Vertical Finite-Difference Scheme and Hybrid Vertical Coordinates, Mon. Wea. Rev., 109, 758–766, https://doi.org/10.1175/1520-0493(1981)109%253C0758:AEAAMC%253E2.0.CO;2, 1981.

Skamarock, W. C., Ong, H., and Klemp, J. B.: A Fully Compressible Nonhydrostatic Deep-Atmosphere Equations Solver for MPAS, Monthly Weather Review, 149, 571–583, https://doi.org/10.1175/MWR-D-20-0286.1, 2021.

Staniforth, A. and White, A. A.: Further non-separable exact solutions of the deep- and shallow-atmosphere equations, Atmosph. Sci. Lett., 12, 356–361, https://doi.org/10.1002/asl.349, 2011.

Thuburn, J., Wood, N., and Staniforth, A.: Normal modes of deep atmospheres. I: Spherical geometry, Quart J Royal Meteoro Soc, 128, 1771–1792, https://doi.org/10.1256/003590002320603403, 2002.

Ullrich, P. A., Melvin, T., Jablonowski, C., and Staniforth, A.: A proposed baroclinic wave test case for deep- and shallow-atmosphere dynamical cores, Quart J Royal Meteoro Soc, 140, 1590–1602, https://doi.org/10.1002/qj.2241, 2014.

Vallis, G. K.: Atmospheric and Oceanic Fluid Dynamics: Fundamentals and Large-Scale Circulation, 2nd ed., Cambridge University Press, https://doi.org/10.1017/9781107588417, 2017.

White, A. A. and Bromley, R. A.: Dynamically consistent, quasi-hydrostatic equations for global models with a complete representation of the Coriolis force, Quart J Royal Meteoro Soc, 121, 399–418, https://doi.org/10.1002/qj.49712152208, 1995.

White, A. A., Hoskins, B. J., Roulstone, I., and Staniforth, A.: Consistent approximate models of the global atmosphere: shallow, deep, hydrostatic, quasi-hydrostatic and non-hydrostatic, Quart J Royal Meteoro Soc, 131, 2081–2107, https://doi.org/10.1256/qj.04.49, 2005.

Wood, N. and Staniforth, A.: The deep-atmosphere Euler equations with a mass-based vertical coordinate, Quart J Royal Meteoro Soc, 129, 1289–1300, https://doi.org/10.1256/qj.02.153, 2003.

Wood, N., Staniforth, A., White, A., Allen, T., Diamantakis, M., Gross, M., Melvin, T., Smith, C., Vosper, S., Zerroukat, M., and Thuburn, J.: An inherently mass-conserving semi-implicit semi-Lagrangian discretization of the deep-atmosphere global non-hydrostatic equations, Quart J Royal Meteoro Soc, 140, 1505–1520, https://doi.org/10.1002/qj.2235, 2014.

Yatunin, D., Byrne, S., Kawczynski, C., Kandala, S., Bozzola, G., Sridhar, A., Shen, Z., Jaruga, A., Sloan, J., He, J., Huang, D. Z., Barra, V., Chew, R., Boral, A., Chen, Y., Knoth, O., Ullrich, P., Mbengue, C., and Schneider, T.: The Climate Modeling Alliance Atmosphere Dynamical Core: Concepts, Numerics, and Scaling, J Adv Model Earth Syst, 18, e2025MS005014, https://doi.org/10.1029/2025MS005014, 2026.

Zängl, G., Reinert, D., Rípodas, P., and Baldauf, M.: The ICON (ICOsahedral Non-hydrostatic) modelling framework of DWD and MPI-M : Description of the non-hydrostatic dynamical core, Quart J Royal Meteoro Soc, 141, 563–579, https://doi.org/10.1002/qj.2378, 2015.

https://doi.org/10.5194/egusphere-2026-2297
Preprint. Discussion started: 5 June 2026

Zhang, Y., Li, J., Yu, R., Zhang, S., Liu, Z., Huang, J., and Zhou, Y.: A Layer-Averaged Nonhydrostatic Dynamical Framework on an Unstructured Mesh for Global and Regional Atmospheric Modeling: Model Description, Baseline
515 Evaluation, and Sensitivity Exploration, J Adv Model Earth Syst, 11, 1685–1714, https://doi.org/10.1029/2018MS001539, 2019.